

Beneath Our Feet: Strategies for Locomotion in Granular Media

A.E. Hosoi¹ and Daniel I. Goldman²

¹Department of Mechanical Engineering, Massachusetts Institute of Technology, Cambridge, Massachusetts 02139; email: peko@mit.edu

²School of Physics, Georgia Institute of Technology, Atlanta, Georgia 30332

Annu. Rev. Fluid Mech. 2015. 47:431–53

First published online as a Review in Advance on September 22, 2014

The *Annual Review of Fluid Mechanics* is online at fluid.annualreviews.org

This article's doi:
10.1146/annurev-fluid-010313-141324

Copyright © 2015 by Annual Reviews.
All rights reserved

Keywords

sand, digging, bio-inspired design

Abstract

“If you find yourself in a hole, stop digging.” Although Denis Healey’s famous adage (Metcalf 2007) may offer sound advice for politicians, it is less relevant to worms, clams, and other higher organisms that rely on their digging ability for survival. In this article, we review recent work on the development of simple models that elucidate the fundamental principles underlying digging and burrowing strategies employed by biological systems. Four digging regimes are identified based on dimensionless digger size and the dimensionless inertial number. We select biological organisms to represent three of the four regimes: razor clams, sandfish, and nematodes. Models for all three diggers are derived and discussed, and analogies are drawn to low-Reynolds number swimmers.

1. INTRODUCTION

Digging and burrowing are pervasive in the animal kingdom. Organisms from ants to armadillos dig for many reasons, including feeding, anchoring, shelter, and protection. Similar to swimming and flying, digging strategies are tightly coupled to the dynamics of the surrounding medium—water for swimmers, air for fliers, and granular media for diggers. Relative to their swimming and flying counterparts, digging organisms present a particularly attractive target of investigation as their environment is largely dominated by frictional interactions between grains in dry substrates or viscous effects in saturated environments. The dissipative nature of these systems can dramatically simplify the dynamics, making quantitative comparisons with macroscopic biological systems feasible.

However, simplification in the analysis of the governing equations comes at a price in other arenas. The first challenge associated with studying digging organisms is seemingly mundane, yet it can be a showstopper. Simply put, it is difficult to see through dirt. To understand the strategies adopted by digging and burrowing animals, it is necessary to visualize the kinematics of fully submerged organisms and, ideally, the accompanying stresses and displacements in the surrounding medium. Furthermore, this visualization must be done dynamically. This can be accomplished by index matching grains and fluids (not ideal as index-matched fluids are often harmful to biological specimens), imaging through thin geometries such as Hele-Shaw cells (Winter et al. 2012) or ant farms (Gravish et al. 2012) (also not ideal as the dynamics of granular materials may be strongly influenced by boundary effects), or X-ray imaging.

A second challenge lies in the derivation of the governing equations of motion. Although it is possible to write down relevant macroscopic averaged conservation laws for digging organisms and devices, the accompanying granular constitutive relationships remain an open topic of investigation.

1.1. Scope of This Review

Locomotion through granular media is a vast topic that encompasses biology, physics, soil mechanics, fluid dynamics, rheology, optimization, and many other disciplines. Each of these fields presents fascinating viewpoints on the topic of digging, and it is impractical to address all of them in a single review article. Hence, we restrict our scope first and foremost to biologically motivated digging strategies, neglecting many digging approaches employed by fabricated devices. Second, we emphasize the physical strategies adopted by biological diggers, rather than detailed physiology, except as it relates to the physics of digging. Third, in the examples that follow, some cases consider fluid-saturated materials, and others dry grains. Rather than a comprehensive review of all possible dry and saturated combinations, we again select the most relevant scenarios motivated by the biological context. Finally, we focus on locomotion through granular media versus on granular media, the latter of which has recently received quite a bit of attention, particularly in the robotics community (Goldman et al. 2009).

1.2. Characterizing Flowing Granular Media

A granular medium is an ensemble of non-Brownian particles that interact through a combination of hydrodynamic interactions (in the case of saturated substrates), interparticle friction, and collisions. Because the particles are non-Brownian and particle interactions are highly dissipative, granular systems are easily trapped in nonequilibrium, metastable states. The nonequilibrium nature of these ensembles makes it challenging to apply classical statistical approaches to derive constitutive relationships. Instead, models are typically constructed via a phenomenological

approach in which the medium is considered a viscoplastic. This approach captures two signatures of granular flow: a flow threshold or yield stress, followed by viscous-like behavior.

Since the pioneering work of Bagnold (1954), many models have been proposed to reflect these features. One of the most successful strategies for describing dense granular flows is the local rheology model. In this model, the granular medium is described as a frictional viscoplastic liquid (Forterre & Pouliquen 2009) with a friction coefficient and local volume fraction that depend only on the inertial number I ,

$$I = \frac{\dot{\gamma} d}{\sqrt{P/\rho_p}}, \quad (1)$$

where ρ_p is the particle density, d is a characteristic grain size, P is a characteristic pressure scale, and $\dot{\gamma}$ is a characteristic shear rate. This quantity, which approximates the relative importance of inertial effects and confining stresses, can be interpreted as the ratio of two timescales: one that characterizes the typical time associated with microscopic particle rearrangements and a macroscopic timescale $1/\dot{\gamma}$ associated with the shear rate. In the context of digging, the inertial number defines three important regimes: quasi-static flow ($I < 10^{-3}$), dense flow ($10^{-3} < I < 10^{-1}$), and collisional flow ($I > 10^{-1}$). Digging typically occurs in one of the first two regimes, which we refer to as slow and fast digging, respectively.

Diggers may also be classified by $S = L/d$, which characterizes the size of the digger relative to the grain size. For our purposes, the term small refers to diggers that are comparable to the grain size, and the term large refers to diggers that are much larger than the grains. This leaves us with four interesting regimes—large and fast, large and slow, small and fast, and small and slow—which are summarized in **Figure 1**, along with representative organisms in each regime.

1.3. Computer Simulation of Dry Granular Media

Although the examples in this review focus on analytical and experimental results, it is important to recognize the key role simulation has played in analyzing digging systems. The discrete element method (DEM) is a useful computational technique in modeling the flow of dry granular media (Poschel 2005) and treats each particle within the simulation as a dissipative repulsive sphere governed by Newton's laws. Each sphere is propelled via collisions with other particles and gravitational effects. In the normal direction of collision, Hertzian contact is typically used to generate repulsion, and a term is added to account for dissipative effects, which can be quantified by the coefficient of restitution. Coulomb friction is used to model sliding contacts, with a static friction term employed to generate statically stable packings. If interaction parameters are chosen correctly, DEM simulations can quantitatively reproduce features of experimental granular flows (Ding et al. 2011) and can thus be used as a microscopic view into grain-level dynamics. DEM simulations are computationally simple to implement relative to analogous computational techniques in fluids flows (e.g., computational fluid dynamics), and simulations of a few million particles can be readily performed on desktop PCs.

2. ANALOGIES WITH LOW-REYNOLDS NUMBER LOCOMOTION

Locomotion through granular media is largely dominated by drag, which immediately invites comparison with other overdamped systems. In particular, it is instructive to examine the similarities (and differences) between digging in granular substrates and low-Reynolds number swimming—a topic that has received considerable attention in the fluid dynamics community (e.g., recently reviewed in Lauga & Powers 2009). The governing equations for the pressure and velocity fields,

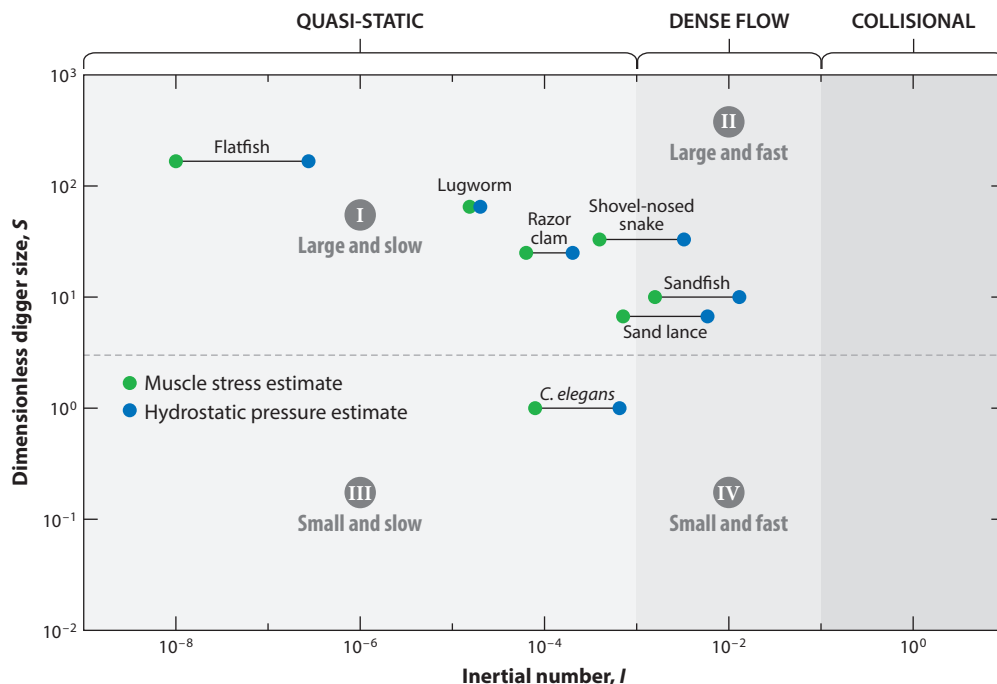


Figure 1

Digging organisms arranged by inertial number I and dimensionless size S . The inertial number was estimated using $\rho = 2,500 \text{ kg/m}^3$ and biologically relevant shear rates and grain sizes. Pressure can be estimated two ways. The first estimate (indicated by the green points) was calculated using characteristic stresses that muscles can produce (approximately 100 kPa). The second estimate (indicated by the blue points) used the hydrostatic pressure at typical burrow depths. Both of these are intended as order-of-magnitude estimates. Four biologically relevant digging regimes are identified by roman numerals.

p and \mathbf{u} , of an incompressible low-Reynolds number flow around a swimming organism in a fluid of viscosity μ are given by the Stokes equations

$$\nabla p = \mu \nabla^2 \mathbf{u}, \quad \nabla \cdot \mathbf{u} = 0, \quad (2)$$

which are linear and independent of time.

2.1. Scallop Theorem

The fact that the Stokes equations possess these two properties leads to a number of interesting consequences in locomotion. First, the locomotion speed V of an organism changing its shape Γ must be linearly proportional to the rate of change of the shape, namely $V = f(\Gamma)\dot{\Gamma}$, where $f(\Gamma)$ is a function of the instantaneous shape of the organism, and the dot indicates a time derivative. If the sequence of shapes is identical under time-reversal symmetry, the organism simply retraces its steps and winds up exactly where it started. Hence, any swimmer that undergoes a reciprocal deformation can never generate a net translation. This inability of reciprocal (non)swimmers was made famous by Purcell (1977) in “Life at Low Reynolds Number,” in which he states “if the animal tries to swim by a reciprocal motion, it can’t go anywhere. Fast or slow, it exactly retraces its trajectory and it’s back where it started.”

Purcell used the scallop—two rigid bodies connected by a hinge—as the canonical example of a swimmer that can undergo only reciprocal deformations, and consequently, this limitation

of low-Reynolds number locomotors has become known as the scallop theorem. “Life at Low Reynolds Number” opened the flood gates for new proposed designs of effective low-Reynolds number swimmers, which typically introduce chirality or additional degrees of freedom to break symmetry. Purcell himself hypothesized the three-link swimmer, the helical swimmer, and the flexible oar, which were all followed by in-depth analyses by other researchers (Becker et al. 2003, Jung et al. 2007, Lauga 2007, Liu et al. 2011, Qian et al. 2008, Raz & Avron 2008, Tam & Hosoi 2007, Wiggins & Goldstein 1998, Yang et al. 2009, Yu et al. 2006); other proposed designs such as the pushmepullyou (Avron et al. 2005) and the waving sheet (Taylor 1951) add to the taxonomy. As shown in the following sections, many observed biological digging strategies are remarkably analogous to the hypothetical strategies that appear in the canon of low-Reynolds number locomotion.

2.2. Resistive Force Theory

Another commonality in inertialess locomotion is that the instantaneous forces and torques on the organism must balance. Typically in locomotion studies, translational velocities are found by balancing drag with relevant propulsive effects, such as vortex shedding or inertia. However, in these highly overdamped systems, drag is often the only available source of propulsion. Hence, locomotion can only arise from anisotropy in the drag forces. In a viscous fluid, the drag force \mathbf{F}_D is well known for common geometries and is linearly proportional to the velocity of the object relative to the fluid:

$$\mathbf{F}_D = \sum_i C_i (\mathbf{V} \cdot \mathbf{e}_i) \mathbf{e}_i, \quad (3)$$

where \mathbf{V} is the relative velocity of the object, \mathbf{e}_i are appropriately chosen unit vectors, and the drag coefficients C_i depend on the geometry of the object. For a translating sphere, one obtains $\mathbf{F}_D = 6\pi a\mu\mathbf{V}$, where a is the radius of the sphere. For a long, slender cylinder, the respective parallel and perpendicular drag coefficients are given by

$$C_{\parallel} = \frac{2\pi\mu}{\ln(L/a) - 1/2}, \quad C_{\perp} = \frac{4\pi\mu}{\ln(L/a) + 1/2}, \quad (4)$$

where L and a are the length and radius of the cylinder, respectively.

Computing drag coefficients for arbitrary geometries is a nontrivial exercise. Hence, locomotion studies frequently employ a resistive force theory (RFT) approximation, as first proposed by Gray & Hancock (1955). This approximation postulates that, for an undulating slender object in which the radius of curvature is large compared to the radius of the filament, each infinitesimal segment is (to first order) hydrodynamically uncoupled from the others. Hence, the drag forces associated with normal and tangential motion are approximately proportional to the local filament velocity, and the drag coefficients can be approximated as those of a straight cylinder, as given in Equation 4. This approximation proves to be particularly useful in granular locomotion, provided one can derive new appropriate drag coefficients in the relevant digging regimes.

2.3. Digging Efficiency

A final theme that emerges in the following analyses is efficiency. Optimization is a common goal in biomechanical studies, and one of the trickiest tasks in these investigations is the determination of a relevant metric or cost function to quantify the property being optimized. In locomotion studies, the two most common metrics are (a) maximizing speed for a given power (sprint) and (b) maximizing efficiency for a given speed (marathon). Both these are relevant to digging, which may be used as an escape mechanism (sprint) or as a foraging or anchoring strategy (marathon).

The first metric, maximizing speed, is straightforward. To define the second, maximizing energetic efficiency or endurance, we note that an actively burrowing animal consumes power as it deforms the surrounding medium and itself, and a certain fraction of that power is transformed into useful unidirectional motion. A typical efficiency η , analogous to the hydrodynamic efficiencies commonly used for low-Reynolds number swimmers, can be defined as the ratio of the power required to drag the digger through the soil at the average digging velocity (namely the useful fraction of the power) to the total power required to deform the substrate Φ :

$$\eta = \frac{\mathbf{F}_D \cdot \mathbf{V}}{\Phi}. \quad (5)$$

As a point of comparison, efficiencies for low-Reynolds number swimmers are typically on the order of a few percent. G.I. Taylor's (1951) swimming sheet, which is a superstar among low-Reynolds number locomotors, can attain efficiencies as high as 7%. As shown in the examples below, diggers can often achieve much higher efficiencies by exploiting asymmetries arising in the environment that can enhance the effectiveness of their nonreciprocal kinematics.

Another common measure of efficiency is the cost of transport (COT), which is defined as the energy consumed to move a unit weight a unit distance, normalized by the weight of the organism or device, times the distance traveled. This metric is commonly used in biomechanical and robotic studies. It is roughly the inverse of the hydrodynamic efficiency defined in Equation 5 in the sense that the denominator of the COT can be interpreted as the useful work performed to move the locomotor, and the numerator is the total energetic cost, which may include food, air, electricity, or gasoline. An excellent summary of the COT for many organisms and devices, from freight trains ($\approx 1.1 \times 10^{-2}$) to mice (≈ 40), is presented in Kuo (2007).

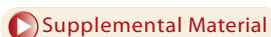
3. MODES OF DIGGING

We now present analyses of specific digging organisms in each of the four digging regimes. There are many biological species one could choose for this purpose, and the examples below were selected partially based on their effectiveness in illustrating key concepts and partially based on the authors' experience in working with these organisms. In all cases, the biological discussion is paired with an analysis of a canonical digger that isolates the principal physical digging mechanisms employed by the biological system.

3.1. Regime I: Big ($S \gg 1$) and Slow ($I \ll 1$)

Regime I is broadly populated by soft burrowers (Trueman 1975). Among these organisms, there are two widely adopted digging strategies: (a) undulatory motions used by worms and chordates and (b) the two-anchor strategy. Undulatory digging is discussed extensively in Sections 3.2 and 3.3; hence, this section focuses on bivalves (e.g., clams), which employ a two-anchor strategy. A bivalve consists of a rigid shell and a soft foot that can protrude into the substrate. These two components form the two anchor points in the animal's burrowing strategy. The two halves of the shell are connected via a torsional spring that opens the shell when the muscles are relaxed. Fraenkel (1927) identified the following key stages in bivalve digging: protrusion of foot into the substrate (*Hakenform*), dilation of the distal end to form an anchor (*Schwellform*), and contraction of retractor muscles to pull the shell into the substrate (*Grabstufe*) (see **Supplemental Video 1**; follow the **Supplemental Material link** from the Annual Reviews home page at <http://www.annualreviews.org>).

These stages are illustrated in **Figure 2a**. In a clam, the foot, shell, and muscles can be thought of as a hydraulic system in which the force produced by the muscles controlling the opening and



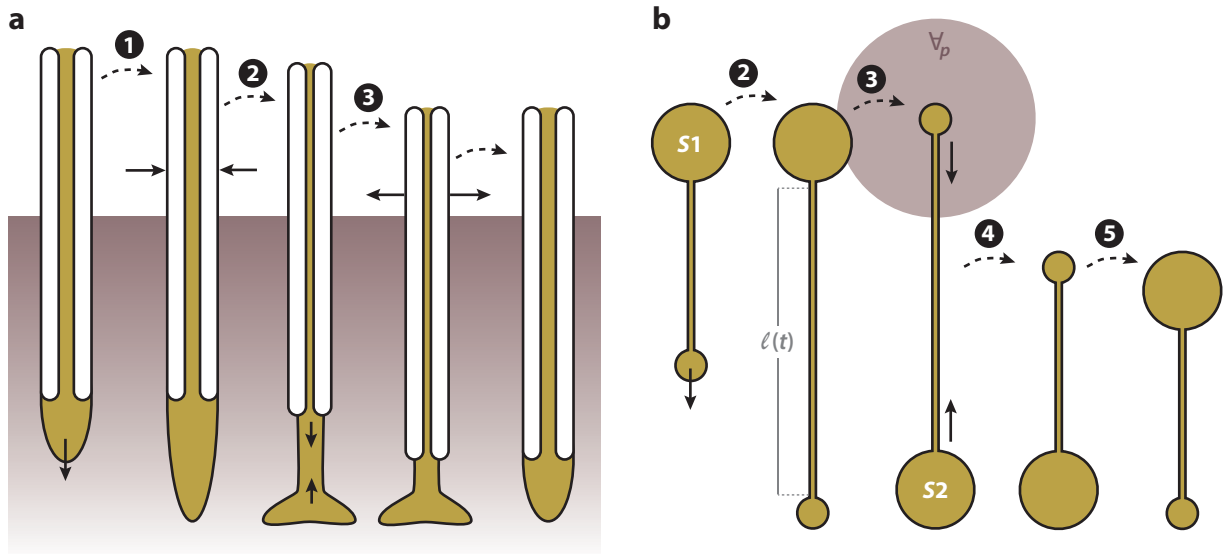


Figure 2

(a) Schematic illustration of the three digging stages in burrowing bivalves: (1) protrusion of foot into substrate, (2) dilation of the distal end to form an anchor, and (3) contraction of retractor muscles to pull the shell into the substrate. (b) Analogous schematic illustration of the digging pushmepullyou. Initially the shell (S1) expands to form the first anchor point. The foot (S2) is then pushed into the substrate. S1 contracts, squeezing fluid into S2, which expands to form a new anchor point. Then the connection between the two spheres contracts, pulling S1 into the substrate. And finally fluid is reversed from S2 to S1, expanding the shell and returning the pushmepullyou to its original configuration.

closing of the shell can be transferred to the substrate. In the first step, the animal relaxes these muscles, and the spring-loaded shell braces against the sand, serving as the primary anchor point. This allows the animal to extend its foot into the substrate. In the second step, the shell squeezes shut, increasing the hydrostatic pressure inside the animal. This increase in pressure drives fluid into the flexible foot, which expands, exerting pressure on the adjacent sand. The expanded foot then serves as the second anchor point and allows the animal to pull the shell into the burrow in the third step.

3.1.1. Canonical analogy: the pushmepullyou. Let us consider an idealized bivalve moving through a saturated granular substrate. The clam can be modeled as a pushmepullyou (Avron et al. 2005), consisting of a spherical foot (S2) and a spherical shell (S1) connected by a rigid bar that can actively elongate or contract (**Figure 2b**). The total volume of the digger is conserved, so as one sphere shrinks, the other grows, mimicking the transport of incompressible fluid within the biological organism. The digging cycle of our pushmepullyou progresses through the stages illustrated in **Figure 2b**.

There are two modes of symmetry breaking that contribute to the net translation of the organism in this example. The first mode is the nonreciprocal kinematics of the pushmepullyou. The second is the asymmetry brought about by the differing effective material properties of the substrate surrounding the shell and the foot. As the shell (or foot) contracts, the grains in the surrounding medium unpack, creating a localized region of fluidized material, which lowers the local yield stress and viscosity of the substrate. This trick of modifying the local environment surrounding a contracting organ is a highly effective digging tactic, and the associated gains can be tremendous.

As an order-of-magnitude estimate, let us consider the energy required to dig, which scales as $E \sim Fb$, where b is the depth of the submerged object, and F is the force required to penetrate the granular medium. This force is proportional to the yield stress σ_y of the substrate, which, for packed beds of sand, typically arises from the frictional contact between grains and is set by the hydrostatic pressure, $\sigma_y \sim \rho gb$. Here ρ is the effective density of the fluid-particle mixture, and g is gravitational acceleration. Hence, the force required to penetrate a packed medium scales linearly with the depth, and the energy expended by the digger scales as the depth squared. In contrast, the force required to move through a viscous fluidized system scales as $F_f \sim \mu(\phi)Va$, which is independent of the depth. As above, V is the digging velocity; a is an appropriate length scale of the digger; and μ is an effective viscosity or resistance, which depends on the local volume fraction of particles ϕ . In this idealized fluidized situation, the energy required to dig scales linearly with the depth; therefore, beyond a critical depth, it always pays to fluidize.¹

This transition from a packed to a fluidized state can be critical to animals, which are constrained by the physiological limitations of muscle. For example, the maximum pulling force that a clam such as *Ensis directus*, commonly known as the razor clam, can exert is approximately 10 N (Trueman 1967). We can contrast this with the force required to submerge a razor clam's shell into the animal's habitat soil. This force can be measured directly, and one finds that, as expected, it increases linearly with the depth at a rate of approximately 5 N/cm (Winter et al. 2012). These measurements imply that, in a packed bed in its native habitat, a razor clam's muscles should be able to submerge the animal to a depth of approximately 2 cm. In reality, live razor clams can dig almost two orders of magnitude deeper than this measurement would suggest (Holland & Dean 1977), a feat that is only possible through localized fluidization, which makes burrowing feasible for these organisms.

We now return to our canonical example and estimate digging velocities and efficiencies of the pushmepullyou shown in **Figure 2b**. To illustrate the physical principles that lead to a net translation, we adapt the calculation in Jung (2010) and consider simple sinusoidal kinematics in which the radius of S1 is prescribed as $R_1(t) = a_0 + \delta_a \cos(\omega t)$, and the length of the connecting rod or muscle oscillates out of phase with the sphere dilation: $\ell(t) = \ell_0 - \delta_\ell \sin(\omega t)$. Because the volume of the total swimmer is conserved, the radius of S2 is necessarily given by $R_2(t) = a_0 - \delta_a \cos(\omega t)$. As argued above in Section 2.2, the sum of all forces—namely, the drag on the spheres—must balance:

$$\sum_i \mathbf{F}_i = 0, \quad \text{where} \quad \mathbf{F}_i = 6\pi R_i(t)\mu_i(t)V_i(t). \quad (6)$$

Here $\mu_i(t)$ is the effective viscosity of the surrounding medium experienced by the i -th sphere, and $V_i(t)$ —which we would like to determine for a given set of material properties and kinematics—is the unknown instantaneous velocity of the i -th sphere.

For small deformations of the digger, we first write the effective viscosity as a function of the local void fraction ϵ , defined as the ratio of volume occupied by the pore fluid to the total volume, and consider small perturbations to the initial void fraction ϵ_0 :

$$\mu_i(t) = \mu_0 + \frac{\partial \mu}{\partial \epsilon}(\epsilon - \epsilon_0) + \dots, \quad (7)$$

where the effective viscosity of the unperturbed substrate is μ_0 . To determine $\partial \mu / \partial \epsilon$, we must select an appropriate constitutive relationship $\mu(\epsilon)$, which depends on the material properties of the medium, the history of the packing, external loadings, and grain geometry (see the sidebar

¹This is, of course, only true if there is a fixed energetic cost associated with fluidization that is independent of the depth.

EFFECTIVE VISCOSITY MODELS FOR SUSPENSIONS

For the estimation of the varying material properties of the substrate surrounding the digging organism, it is often reasonable to consider a saturated granular substrate and model it as a suspension with viscosity $\mu = f(\phi)$, where ϕ is the volume fraction of the particles, and the function $f(\phi)$ may blow up at some critical concentration below the maximum packing fraction. There is a tremendous literature on this topic, starting with Einstein's (1906) calculation in which he computed the first correction to the viscosity—which is linear in the particle concentration—in the limit of dilute suspensions. Since then, many studies have empirically measured constitutive relationships, or computed effective viscosities theoretically, or both (Batchelor & Green 1972, Eilers 1941, Ferrini et al. 1979, Frankel & Acrivos 1967, Krieger & Dougherty 1959, Maron & Pierce 1956). There is a rich history associated with this topic that we do not address in this review, as the qualitative conclusions related to digging do not sensitively depend on the details of $f(\phi)$.

Effective Viscosity Models for Suspensions). One can compute the change in void fraction, $\epsilon - \epsilon_0$, by defining \forall_p as the characteristic volume of the perturbed soil, the extent of which depends on the geometry of the burrowing organism and initial soil properties. A straightforward geometric calculation for small digging deformations, namely $\delta_a \ll a_0$, leads to

$$\epsilon - \epsilon_0 = \frac{4\pi}{3\forall_p}(1 - \epsilon_0)[a_0^3 - R_1^3(t)] + \dots \approx \delta_a \frac{4\pi a_0^2}{\forall_p}(1 - \epsilon_0) \cos(\omega t). \quad (8)$$

Finally, to close the system, we note that the sphere velocities are related by a kinematic constraint: $V_2 = V_1 + \dot{\ell}$. The force balance equation can now be solved for the velocity of S1, which is then averaged over one digging cycle, yielding the average translational velocity of the organism:

$$\bar{V} = \frac{\pi}{2}(\omega \delta_\ell) \frac{\delta_a}{a_0} \left(1 - \frac{k_0}{\mu_0}\right), \quad \text{where} \quad k_0 \equiv \frac{\partial \mu}{\partial \epsilon} \frac{4\pi a_0^3}{\forall_p}(1 - \epsilon_0). \quad (9)$$

Tying this back to the two types of symmetry breaking discussed above, the first term in the average digging velocity represents translation owing to the nonreciprocity of the kinematics. The second represents the net motion that arises from the asymmetric material properties of the environment surrounding the spheres. This calculation can be repeated with a slightly more realistic geometry in which the shell is modeled as a cylinder, which allows one to address a number of interesting questions, such as computing the optimal aspect ratio of a clam shell (Jung et al. 2011).

Although digging speed is paramount for organisms that use burrowing as an escape mechanism, others may employ digging in other capacities—such as foraging—which may elevate energetic efficiency to the primary goal. Consider the digging efficiency η defined in Section 2.3. The power in the denominator required to deform the substrate can be written as the sum of the power required to move the individual spheres through the medium and the power P_i dissipated by the expanding (or shrinking) spheres. The power associated with dilation P_i can be estimated as the product of the local stress and the dilation rate. Estimating the stress as $\sigma = 2\mu(t)\partial \dot{R}/\partial r = 4\mu(t)\dot{\forall}/(3\forall)$, one can calculate the hydrodynamic efficiency of the granular pushmepullyou to lowest order as

$$\eta = 6\pi \left(1 - \frac{k_0}{\mu_0}\right)^2 \left(\frac{\delta_a}{a_0}\right)^2 \frac{\delta_l^2}{3\delta_l^2 + 32\delta_a^2}. \quad (10)$$

In this estimate, the efficiency increases as both δ_l and δ_a increase. However, recall that this approximation is only valid for small δ_a and in the limit that local variations in viscosity can be well approximated by the first term in the expansion in Equation 7. Again the calculation can be

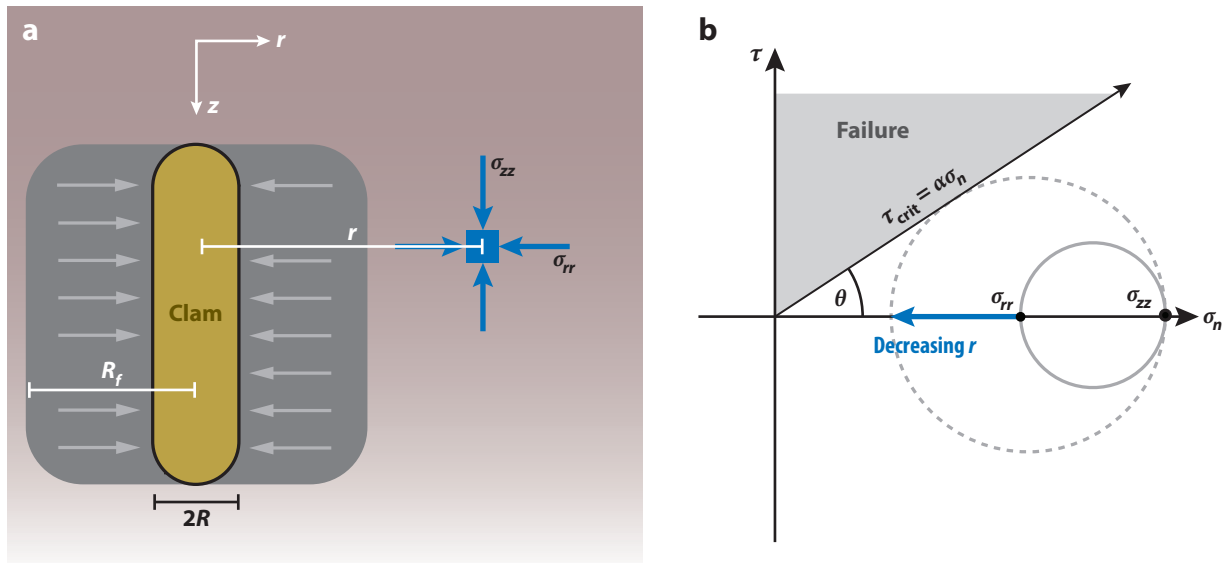


Figure 3

(a) Schematic illustration of a cylindrical digging clam and local state of stress in the substrate. (b) Mohr's circle, illustrating the graphical identification of the failure zone. Larger circles correspond to smaller values of r , indicating neighborhoods closer to the clam.

repeated for a cylindrical shell to determine optimal aspect ratios for efficient digging (Jung et al. 2011).

3.1.2. Finite yield stress substrates. In the analysis above, we lump the characteristic volume of the perturbed soil into a single unknown parameter, \forall_p . In general, this volume may be a complicated function of the soil properties; however, for a simple finite yield stress material (e.g., a Bingham plastic), \forall_p can be estimated by calculating the location of the yield or failure surface around the digger. To illustrate this concept, we consider a long, axisymmetric cylindrical clam shell (**Figure 3a**). Closing of the shell is modeled as a decrease in the radius of the cylinder R . As the radius decreases, the horizontal stress in the medium surrounding the organism decreases. (From here on, we use the sign convention commonly used in soil mechanics, in which compressive stresses are positive.) When this stress drops below a critical value, the soil fails.

To calculate the location of the failure surface, we first need to estimate the stresses in the granular bed as they relate to the kinematics of the organism. Let us consider the vertical and horizontal stresses a distance r from the clam, as shown in **Figure 3a** (by symmetry, there are no shear stresses in this configuration). In a saturated medium, the vertical stress is a combination of the hydrostatic pressure, $\sigma_{hs} = \rho g z$, and pore pressure, which arises from the lubrication forces between particles, $p_{pore} = \rho_f g z$. As above, ρ is the effective density of the fluid-particle mixture, namely $\rho = \rho_p \phi + \rho_f (1 - \phi)$; g is gravitational acceleration; ρ_p is the particle density; and ρ_f is the fluid density. Hence, the vertical stress can be written as

$$\sigma_{zz} = \sigma_{hs} - p_{pore} = \phi(\rho_p - \rho_f)gz. \quad (11)$$

In equilibrium, the horizontal stress, σ'_{rr} (without the pore pressure correction), can be found by solving $\nabla \cdot \sigma' = 0$ with boundary conditions $\sigma'_{rr} = p_0$ at $r = R$, where p_0 is determined by the

kinematics of the shell, and $\sigma'_{rr} \rightarrow \sigma_\infty$ as $r \rightarrow \infty$. The resulting expression for σ'_{rr} again needs to be corrected to account for the pore pressure, namely $\sigma_{rr} = \sigma'_{rr} - p_{\text{pore}}$, which leads to the following expression for the effective horizontal stress (Landau & Lifshitz 1984):

$$\sigma_{rr} = \frac{R^2}{r^2}(p_0 - \sigma_\infty) + \sigma_\infty - \rho_f g z. \quad (12)$$

The only remaining unknown quantity is σ_∞ , the horizontal stress in the far field, which can be measured. In general, soil engineers do not measure σ_∞ ; rather, they report K_0 , the coefficient of lateral earth pressure. This is a property of the substrate that depends both on the history of the soil and on the material properties of the granular medium. In unperturbed soil (i.e., no clam), one obtains $\sigma_{rr} = K_0 \sigma_{zz}$, which defines K_0 (Lambe & Whitman 1969, Terzaghi et al. 1996).

Given this picture of the stress state in the surrounding medium, one can address the original question of estimating \forall_p by computing zones of failure in the granular substrate. As a first estimate, we select one of the simplest empirical failure criteria, namely that the critical shear stress at which the material yields is proportional to the normal stress, $\tau_{\text{crit}} = \alpha \sigma_n$. This criterion can be graphically evaluated using Mohr's circle to transform the local state of stress (**Figure 3b**) (Wieghardt 1975). As the clam closes its shell, the horizontal stress decreases, which moves the minimum principal stress to the left in **Figure 3b**. As Mohr's circle grows, it intersects the failure criterion at some critical value of σ_{rr} . This critical value corresponds to a physical radius located a distance R_f from the clam, and the soil within this critical radius yields. The failure radius can now be deduced geometrically via this intersection point. From the diagram in **Figure 3**, we see that $\sin \theta = \sigma_M / (\sigma_{rr} + \sigma_M)$, where $\sigma_M = (\sigma_{zz} + \sigma_{rr})/2$, which implies that, at the failure surface,

$$\sigma_{zz} = \frac{1 + \sin \theta}{1 - \sin \theta} \sigma_{rr}, \quad (13)$$

where θ is the angle of repose of the granular medium, and σ_{zz} and σ_{rr} are given in Equations 11 and 12, respectively.

Combining Equation 13 with our expressions for horizontal and vertical stresses, we find that the dimensionless failure radius, R_f/R , is defined by

$$\frac{R_f^2}{R^2} = \frac{\beta}{\beta K_0 - 1} \left[K_0 + \frac{\rho_f}{\rho - \rho_f} \left(1 - \frac{p_0}{p_{\text{pore}}} \right) \right], \quad (14)$$

where $\beta \equiv (1 + \sin \theta)/(1 - \sin \theta)$. As $z \rightarrow \infty$ (i.e., the clam burrows deeper), one finds that $p_0/p_{\text{pore}} \rightarrow 0$, so R_f approaches a constant value. For glass beads, a favorite medium of granular physicists, one obtains $K_0 = 0.5$ and $\theta = 35^\circ$, and the dimensionless failure radius approaches $R_f/R \approx 3.3$ for large z . In fact, for a wide variety of soil parameters, Equation 14 predicts that the failure radius lies between roughly 1 and 3 digger radii, which is consistent with the limited available biological data and implies that fluidization is a fairly localized phenomenon for these slow diggers. This prediction has also been tested using a robotic digger, RoboClam; measurements confirm that fluidization is localized to within a few device radii (Winter et al. 2014).

3.2. Regime II: Big ($S \gg 1$) and Fast ($I \gg 1$)

In regime II, a swimmer's characteristic thrusting surface dimensions are larger than the grain diameter, and motion occurs at speeds that typically generate $I > 10^{-3}$ when the digger is fully submerged. Biologically, in dry media, this regime is home to sand swimmers (see **Figure 4**) classified by the biologist Mosauer (1932) as subarenaceous, implying that they move within dry noncohesive granular media (e.g., desert sand) typically several body diameters below the surface.

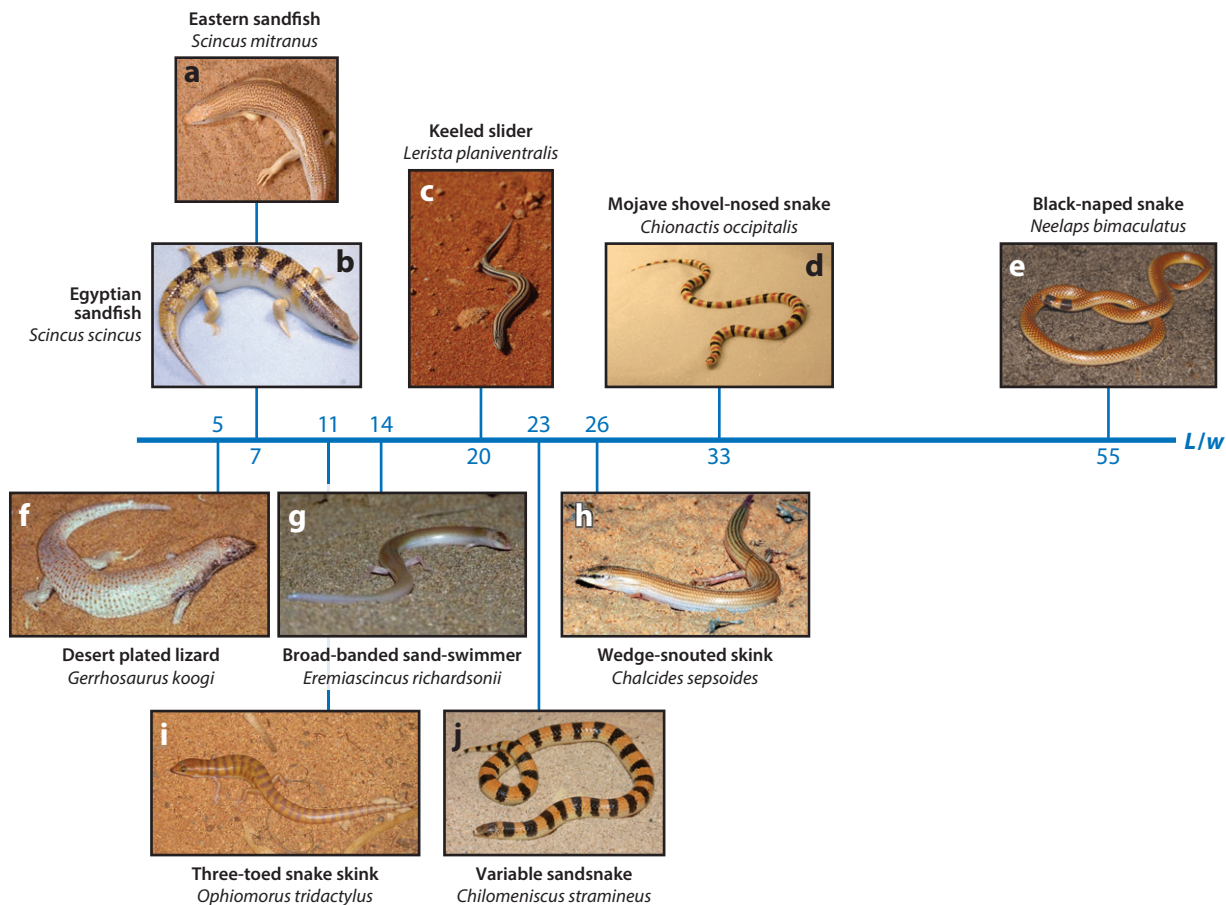


Figure 4

Subarenaceous desert snakes and lizards organized by aspect ratio, where w is the characteristic width of the animal, and L is the characteristic length. Panel *a* courtesy of Alexey Sergeev; panel *b* courtesy of Daniel Goldman; panel *c* courtesy of John Sullivan, Creative Commons; panel *d* courtesy of Daniel Goldman; panel *e* courtesy of Simon Cherriman; panel *f* courtesy of Paul Freed; panel *g* courtesy of Wikimedia user Kelapstick; panel *h* courtesy of Gabriel Martínez del Mármol Marín; panel *i* courtesy of Omid Mozaffari; and panel *j* courtesy of William Flaxington.

Before we discuss the biological organisms, we consider a granular version of Purcell's three-link swimmer as it illustrates how traveling waves create movement in granular media in this regime and highlights some surprising similarities of granular swimming to locomotion at low Reynolds numbers.

3.2.1. Canonical analogy: the three-link swimmer. In regime II, DEM simulation can prove useful to understand features of digging. Using a multibody simulation coupled to a DEM simulation capable of tracking boxes of $\sim 10^6$ particles, Goldman and colleagues simulated a sand-swimming robot in a large bed of 6-mm plastic particles (Maladen et al. 2011a,b). Goldman's group also used this tool to model the locomotion of a sandfish moving through relatively large particles and compared it to the movement of the live organism in a similar environment (Ding et al. 2012, Maladen et al. 2011a).

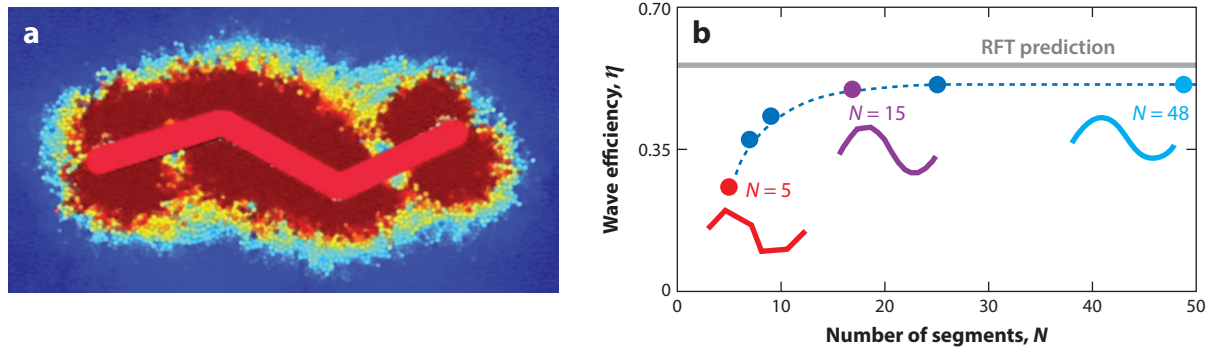


Figure 5

Robotic swimming in a frictional fluid (regime II). (a) A three-link swimmer moving forward in a discrete element method simulation within a granular medium comprising 6-mm plastic spheres; only a single plane is shown. The particles are colored by instantaneous speed [slow (*blue*) to fast (*red*)]. The fluid extends approximately a single body width away from the swimmer. (b) Effects of increasing the number of segments N in the simulated swimmer on the wave efficiency η , the ratio of forward swimming speed to backward wave speed (*thick gray line*). Panel *b* adapted with permission from Maladen et al. (2011b). Abbreviation: RFT, resistive force theory.

These DEM simulations reveal that a defining characteristic of regime II is a continuously fluidized region of material surrounding the organism (see **Figure 5**) (Ding et al. 2012, Maladen et al. 2011a); thus, a swimmer moves within a self-generated localized frictional fluid such that the grains are mobile, but Coulomb friction forces (instead of viscous forces) dominate inertia. Measuring particle speeds in DEM (see **Figure 5**) reveals that the fluid region decays within roughly a body width away from the swimmer.

The insight from DEM motivates the use of RFT in regime II, a fortunate situation as RFT is much faster to calculate (seconds versus days) and can yield to analysis. DEM simulations also reveal that such swimming systems are kinematic, and thus the conditions established by Shapere & Wilczek (1987) (e.g., symmetry, gauge invariance) are satisfied, at least in a horizontal plane. With these assumptions, Goldman and colleagues (Hatton et al. 2013) recently analyzed regime II swimming of a Purcell three-link swimmer using tools of geometric mechanics originally developed in the robotics community (Hatton & Choset 2011, Ostrowski & Burdick 1998). This approach gives geometric insight into optimal deformation patterns and facilitates comparison between swimming in regime II granular media and low-Reynolds number fluids.

To apply RFT in regime II, we require force relations for dry granular media, the analog to Stokes equations in Newtonian fluids. Because theory cannot yet provide these, Goldman's group measured drag forces on cylinders (Maladen et al. 2009, 2011a) immersed in granular media at a fixed depth, varying the angle of attack, depth, and speed. The relationships are plotted in **Figure 6**. These force relations differ from those of a viscous fluid in that they are insensitive to speed, and perpendicular forces rise more steeply at shallow attack angles of elemental intruders. Unlike forces in a fluid, the drag force increases with the depth into the medium; this makes it relatively simple to calculate with the RFT at fixed depths but certainly adds to the challenge of modeling locomotion as an animal descends into the medium.

For ease of calculation, the curves in **Figure 6** can be approximated by the following expression: For a segment of a cylinder with length ds , radius r , velocity $\hat{\mathbf{u}}$, and in-plane normal and tangent vectors $\hat{\mathbf{n}}$ and $\hat{\mathbf{t}}$, the infinitesimal force is

$$d\mathbf{F} = 2k\rho g r \langle z \rangle [f(\hat{\mathbf{n}} \cdot \hat{\mathbf{u}})\hat{\mathbf{n}} + (\hat{\mathbf{t}} \cdot \hat{\mathbf{u}})\hat{\mathbf{t}}]ds, \quad (15)$$

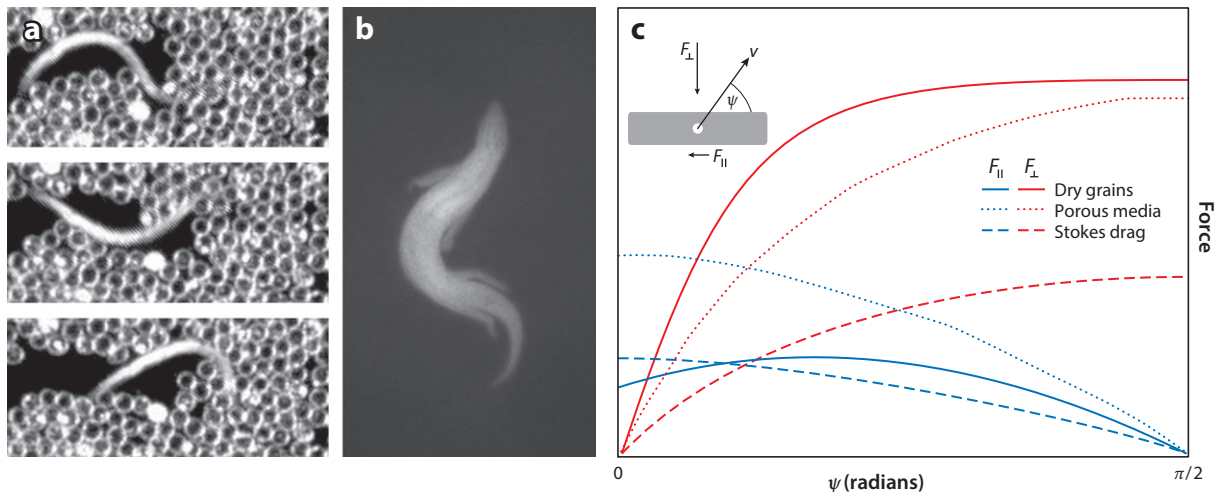


Figure 6

(a) *Caenorhabditis elegans* moving through glass beads. Panel a courtesy of Sunghwan Jung. (b) X-ray image of a sand-swimming sandfish, *Scincus scincus*. (c) Resistive force relations for F_{\perp} and F_{\parallel} as a function of the orientation of the long axis of a cylinder relative to the motion direction. Porous media curves are simply the viscous curves rescaled by a factor that depends on the permeability of the substrate. Red and blue curves correspond to F_{\perp} and F_{\parallel} , respectively. Panel c adapted with permission from Hatton et al. (2013) using data presented in Maladen et al. (2009, 2011a).

where the anisotropy factor is given by

$$f(\mathbf{n} \cdot \hat{\mathbf{u}}) = \left(1 + \frac{C}{\sqrt{\tan^2 \gamma_0 + (\mathbf{n} \cdot \hat{\mathbf{u}})^2}} \right), \quad (16)$$

and C and γ_0 are measured coefficients. For 0.3-mm glass particles, one obtains $C = 1.8$ and $\gamma_0 = 13.8^\circ$. Inputting these relations into the regime II RFT yields predictions that agree with experiments, even for relatively large-amplitude undulations of the three-link granular swimmer (Hatton et al. 2013).

The geometric structures produced by the geometric mechanics theory, the so-called local connection (Bloch 2003) and curvature constraint functions (Hatton et al. 2011, 2013), are qualitatively similar in granular and low-Reynolds number locomotion, facilitating comparison between these situations. For example, the structure of the curvature constraint functions demonstrates why the pattern for optimal movement in granular media is quite similar to that of a low-Reynolds number swimmer (Tam & Hosoi 2007) but also reveals how the larger F_{\perp} in granular media leads to greater displacement per undulation. The agreement between theory and experiment also implies that a scallop theorem should exist for regime II granular locomotion, a topic that should be investigated further in light of recent theoretical insights (Lauga 2011).

3.2.2. Effects of body shape. None of the animals that live in deserts resembles a three-link swimmer. A better approximation of these swimmers is the sand-swimming robot Goldman's group has constructed and systematically studied (Maladen et al. 2011b). This physical model of the sandfish consists of six connected servo motors that can be driven to generate traveling waves to swim in a granular medium of 6-mm-diameter plastic spheres. Goldman's group has also created a DEM simulation of the swimmer that matches experimental measurements over a wide range of conditions (Maladen et al. 2011a,b).

In both experiments and simulations, waves that propagate down the body—head to tail—result in sand swimming. The wave efficiency of the robot (the forward speed relative to the wave speed) is lower than that of the animal (0.35 versus 0.5), but as the number of segments increases (in simulation), the robot's performance improves and approaches the wave efficiency prediction of the RFT for a single-period smooth sinusoidal wave (see **Figure 5**). Thus, this gives us confidence that the RFT can be used to understand the movement of biological swimmers.

To that end, we now discuss the movement strategies of two animals whose kinematics have been studied in detail by Goldman's group, the sandfish lizard (*Scincus scincus*) and the shovel-nosed snake (*Cbionactis occipitalis*) (**Figure 4**). The sandfish is relatively short and stout (an average aspect ratio of $L/w \approx 7$), has legs, runs on surfaces, and dives into the substrate rapidly. The shovel-nosed snake is long and slender (an average aspect ratio of $L/w \approx 30$), typical of many elongated desert snakes and lizards (Norris & Kavanau 1966).

To make the first visualizations of subsurface movement of these subarenaceous organisms, Goldman's group placed a fluidized bed of granular media (0.3-mm-diameter glass spheres, approximating material in dry deserts) between an X-ray source and image intensifier detector; such an apparatus allows visualization of movement with millisecond resolution through 10–20 cm of granular media. Opaque markers were bonded to the scales of the animals along the midlines and legs when applicable to aid in imaging. Markers were tracked to subpixel accuracy using custom software, allowing quantification of body curvature, wave numbers, etc. (see Sharpe et al. 2014a for details).

Because these animals encounter granular material of varying volume fraction in their natural habitats, $0.57 < \phi < 0.63$, Goldman's group pioneered the use of air fluidized beds to prepare substrates into uniform states of different ϕ . Such states have qualitatively different rheological properties upon intrusion. For example, loosely packed material (low ϕ) compacts during interaction, whereas closely packed material dilates; at an intermediate ϕ , called the granular critical state, the material does not experience a net volume change. The volume changes of the material lead to either smooth intrusion forces or periodic fracturing of the material at the initiation site. The resistance forces in high- ϕ material are nearly a factor of two greater than those in low- ϕ material.

Goldman and colleagues discovered that once they are subsurface,² both animals swim by propagating head to tail traveling waves of curvature down the body (see **Figure 7** and **Supplemental Video 2**). Remarkably, the locomotor behaviors are similar in material of different ϕ , although the energetics change (as estimated by the theory). The wave used by the sandfish can be well approximated by a single-period sinusoidal wave. The spatial form of the wave does not change with compaction, depth beneath the surface, or wave frequency. Increasing wave frequency is correlated with increasing swimming speeds, which can reach up to two body lengths per second. The shovel-nosed snake swims more slowly and typically generates approximately 3.5 waves along its body; these waves are better approximated by serpenoid curves. Interestingly, the ranges of maximum wave curvatures used by both the shovel-nosed snake and sandfish are similar.

Another difference between the shovel-nosed snake and sandfish swimming is the amount of slip during locomotion, which we quantify by calculating the angle β_s between the local tangent and segment velocity vectors at every marker along the body during subsurface movement,

$$\beta_s = \cos^{-1}(|\hat{\mathbf{v}}_{t,m} \cdot \hat{\mathbf{T}}_{t,m}|), \quad (17)$$

²We do not discuss the more complex behaviors during initial burial in these and other animals (Jayne & Daggy 2000) in this review.

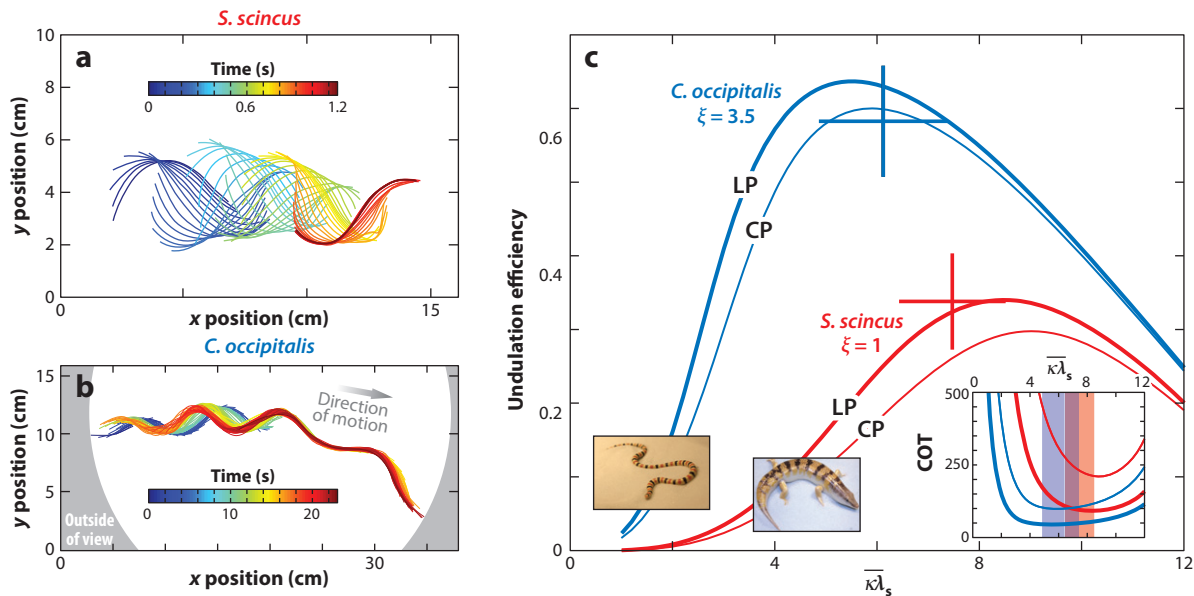


Figure 7

Comparison of locomotor strategies in two regime II sand swimmers: the sandfish (*Scincus scincus*) and shovel-nosed snake (*Chionactis occipitalis*). (a,b) Both move forward through propagation of backward traveling waves of body curvature, although the shovel-nosed snake shows lower slip than the sandfish, as indicated by midline tracings. (c) Undulation efficiency (wavelength-normalized forward distance traveled per undulation cycle) for both animals as predicted in regime II resistance force theory as a function of the normalized average body curvature, using parameters measured in animal experiments, for loosely packed (LP) and closely packed (CP) granular media. Crosses show experimental measurements. (Inset) The mechanical cost of transport (COT). Shaded regions indicate curvatures used by both animals. Figure adapted with permission from Sharpe et al. (2014a).

where $\hat{\mathbf{v}}$ is the unit velocity vector and $\hat{\mathbf{T}}$ is the tangent vector at a body location m and time t . We have discovered that the spatial and temporal average of the slip angle $\bar{\beta}_s$ is a useful metric for locomotion that is not necessarily composed of a uniformly traveling wave. Remarkably, in either animal, $\bar{\beta}_s$ does not change with compaction or depth. In the sandfish, $\bar{\beta}_s$ is a factor of three larger than in the shovel-nosed snake, as can be seen in the track images in **Figure 7**. And because $\bar{\beta}_s$ for both animals is finite, we can assume that the animals are surrounded by a frictional fluid, which motivates the use of the regime II RFT.

The kinematics measured from live animals were used as inputs to the theory to perform the RFT calculations for the shovel-nosed snake and sandfish. The key biological hypothesis is that the neuromechanical control system will act to control the shape of the body to target a particular waveform. Goldman's group made muscle activity measurements in the back of the swimming sandfish (Sharpe et al. 2012), and findings support this hypothesis; the muscle activity increases with the depth into the medium and is independent of the speed (as befitting a frictional fluid swimmer). Intriguingly, the back muscle activity does not depend on compaction; we speculate that this is because a large portion of the drag in closely packed material is on the head, which then generates a frictional fluid around the body whose properties are those of the critical state, independent of initial conditions.

RFT predicts average swimming properties; for example, it predicts $\bar{\beta}_s$ values to 20%. However, detailed comparison between RFT and DEM (Ding et al. 2012, Maladen et al. 2011a) for sandfish swimming reveals that the noninertial assumption is not perfect (as expected in the dense flow

regime). In addition, a hysteresis effect results in an overestimate of RFT forces: Although RFT force relationships are obtained in the steady state of cylinder drag, DEM simulation reveals that, in 3-mm glass particles, the steady state is never achieved owing to the reversals in direction during undulatory swimming. We note that when reversals do not occur, such as in legged locomotion on granular media, agreement between RFT and experiments is excellent over a wide range of parameters (Li et al. 2013). Surprisingly, these results indicate that, unlike in true fluids (Rodenborn et al. 2013), the superposition ansatz in granular RFT is an excellent approximation, even in regimes in which segments are close.


Regime II granular RFT reveals that the animals use kinematics (e.g., curvature and number of waves along the body) that maximize swimming speed and minimize energy use (Sharpe et al. 2012, 2014a). Analysis of the theory (Maladen et al. 2011a) reveals that the optima result from a competition of increased thrust with increasing curvature and a decrease in a forward component of movement at high curvatures (see **Figure 7**). Relative to the sandfish, the shovel-nosed snake achieves lower slip, higher undulatory efficiency, and lower mechanical COT (its skin friction is also a factor of two smaller than that of the sandfish). We speculate that a high undulatory efficiency is important for the sandfish during its rapid (and likely anaerobic) escape behavior, whereas low COT should be useful for the shovel-nosed snake, which burrows slowly. We note that locomotor behaviors such as turning and ascending to the surface remain unexplored.

Finally, we comment on the applicability of regime II RFT to swimming in fully water-saturated granular media. Sand lances (family *Ammodytidae*) are fishes that burrow into fully saturated granular media at the ocean floor. Gidmark et al. (2011) used X-ray imaging to record the burial and subsurface locomotion of these animals. Their study reveals that once submerged, the sand lances swim within the granular media using a head to tail traveling wave of curvature comparable to the sandfish lizard and shovel-nosed snake and with approximately 1.5 wave periods along the body (compared to 1 wave period for the sandfish and 3.5 wave periods for the shovel-nosed snake). We predict that dry granular media RFT can be used to model this locomotion, likely with scaled F_{\parallel} . This would explain how the sand lance can generate small slip using the observed kinematics; however, measurements of force relations in fully saturated granular media are needed to test this hypothesis. In partially saturated systems, surface tension may supply a cohesive force between grains, adding additional complexities that are beyond the scope of this review (see the sidebar Cohesive Media).

3.3. Regime III: Small ($S \sim 1$) and Slow ($I \ll 1$)

In regime III, propulsive strategies are dominated by interactions with individual grains. Our example organism in this regime is *Caenorhabditis elegans*, which has a worm-like shape and is commonly found in saturated soils. Owing to its simple structure and ease of use in laboratory settings, *C. elegans* is one of the most widely used model organisms in modern biology. Although there are many studies related to *C. elegans* swimming in a fluid environment, less is known about its locomotion through granular media, which ironically more closely resembles its natural habitat. The few studies that investigate *C. elegans* in granular settings universally find that locomotion is more effective in granular media than in purely viscous environments. In the following sections, we focus on a few key studies: locomotion through microstructured environments (Majmudar et al. 2012, Park et al. 2008) and motion through a saturated granular medium (Jung 2010) (see **Supplemental Video 3**).

3.3.1. Canonical analogy: undulating slender body. To illustrate the physical principles associated with this regime, we consider an undulating slender body moving through a saturated

 **Supplemental Material**

COHESIVE MEDIA

A great diversity of terrestrial animals locomotes within soils, including within granular material that is not completely dry. For example, the ocellated skink (*Chalcides ocellatus*), which resembles and coexists with the sandfish in the sand dunes of North Sinai, Egypt (Attum et al. 2007), is commonly found near vegetation and harder soil, whereas the sandfish is found further from vegetation on the dry, loose sands of the dunes. Goldman and colleagues developed a systematic method to create repeatable homogeneous locomotion test beds of wet granular media using a shaking/sieving system (see Sharpe et al. 2014b for details). Drag measurements in wet 0.3-mm glass particles reveal that resistance forces increase with depth and, for a given depth, double when the water content, W (the mass of water/mass of granular media), increases by just 3%. These force changes are attributed to the formation of liquid bridges between grains (Kudrolli 2008). To determine if subsurface locomotion is affected by W , Sharpe et al. (2014b) used X-ray imaging to study burial kinematics in the ocellated skink. Relative to the sandfish, movement was slow, taking on average 30 s to enter dry or wet material. In both substrates, the animal moved using a start-stop motion as a wave of body curvature propagated from head to tail. During movement, the head oscillated, and the forelimb on the convex side of the body was used to push the animal forward. Slip was minimal in both wet and dry media, and the final burial depth was correlated with the drag resistance. We hypothesize that analogous to the annelid worm *Nereis virens* (Dorgan et al. 2005, 2007), which cracks the cohesive media as it digs to minimize energy expenditure, the head oscillation decreases the penetration resistance.

environment. In principle, this body could take any smooth continuous shape, but the key physical mechanisms can be illuminated by selecting simple sinusoidal kinematics. In the following, we mirror the calculation performed by Jung (2010) and prescribe the deformation of the centerline of our slender digger as $y(x, t) = (A/2) \cos[(2\pi/\lambda)(x + V_{\text{wave}}t)]$, where A is the amplitude of the undulation, λ is the wavelength of the undulation, and V_{wave} is the propagation velocity of the wave, all of which are selected by the animal. As above, the resulting digging velocity, V , is determined by balancing forces along the organism, and we again turn to RFT to estimate the drag force:

$$\mathbf{F}(s) = C_{\parallel}(\mathbf{u} \cdot \hat{\mathbf{t}})\hat{\mathbf{t}} + C_{\perp}(\mathbf{u} \cdot \hat{\mathbf{n}})\hat{\mathbf{n}}, \quad (18)$$

where s tracks the distance along the centerline; $\hat{\mathbf{t}}$ and $\hat{\mathbf{n}}$ are unit tangential and normal vectors to the body's centerline, respectively; $\mathbf{u} = \mathbf{u}(s, t)$ is the local velocity of the organism; and C_{\parallel} and C_{\perp} are parallel and perpendicular drag coefficients, respectively. To find the total force on the organism, we integrate \mathbf{F} along the body. This calculation can be simplified in the limit of small deformations, namely $A \ll L$. Balancing forces in the $\hat{\mathbf{x}}$ direction yields $\int \mathbf{F} \cdot \hat{\mathbf{x}} dx = 0 \approx C_{\parallel}(I_1 V_{\text{wave}} - I_2 V)L$, which can be rearranged to find the final dimensionless digging velocity

$$\bar{V} = \frac{(C - 1)\delta^2}{1 + C\delta^2}, \quad (19)$$

where \bar{V} has been rescaled by the wave velocity, $\bar{V} = V/V_{\text{wave}}$; C is the ratio of drag coefficients, C_{\perp}/C_{\parallel} ; and δ is a dimensionless deformation amplitude, $\pi A/(\lambda\sqrt{2})$. As noted by Taylor (1951) in his analysis of swimming sheets, the digging velocity calculated in Equation 19 scales as the waving amplitude squared, which can be argued by symmetry. Note that so far we do not make any assumptions that would distinguish digging from swimming, and Equation 19 applies equally well to saturated granular and viscous fluid environments. All the environmental details are captured in the constant parameter, C . This is distinct from the dry granular calculation in the previous section in which the drag coefficients depend on the instantaneous angle of attack and hence are not independent of the kinematics.

The distinction between swimming and digging arises here in the computation of the environmental parameter, C . To estimate C for a wet granular material surrounding a slender cylinder, Jung (2010) proposed to revisit the well-established viscous drag calculation but to model the granular environment as a porous medium. In this case, one can replace the Stokes equation with the Darcy-Brinkman model in which $\nabla p = \mu(\nabla^2 - \alpha^2)\mathbf{u}$. By analogy to unsteady Stokes flow around a cylinder, Jung calculated a modified expression for the drag ratio in the limit of large α :

$$C = \frac{\alpha L + 4}{2}. \quad (20)$$

Estimating α for various particle configurations, Jung predicted RFT velocities that compare well with data from live *C. elegans*.

3.3.2. Locomotion through microstructured environments. More recently, Majmudar et al. (2012) proposed an alternate approach to rationalize the locomotion of *C. elegans* through soils by measuring and modeling passage through structured media. The authors constructed an artificial two-dimensional soil out of a fixed array of pillars saturated with interstitial fluid. In this environment, the undulating body must interact with discrete elements of the embedded microstructure (so-called sand grains). These interactions lead to local hydrodynamic and contact forces experienced by the swimmer that are not incorporated in the continuum-level models described above. Experimental observations are complemented with a model digger, which is represented as an inextensible chain of N elastically linked spherical particles. Unlike the other studies described in this review, the authors prescribed internal forces and torques rather than kinematics, which constitutes a more faithful representation of the biological system. Force and torque balance equations are coupled with the Stokes equations, which are solved numerically; hence, no RFT approximations are required.

Thus equipped with an experimental platform and numerical model, Majmudar et al. (2012) proceeded to investigate the role of various parameters. They found that the speed and path of locomotion through the pillars are strongly dependent on the lattice spacing and the degree of confinement. Consistent with previous biological studies (Park et al. 2008), the authors found that digging speed increases by almost an order of magnitude relative to locomotion through unstructured environments when the ratio of pillar spacing to the worm's length is approximately 0.47. This optimal environment for digging arises owing to a resonance in which the rate of arrival of the pillars is matched with the frequency of undulations, allowing the organism to gain traction by pushing off of fixed structures. With regard to the efficiency defined in Section 2.3, the authors found that as the lattice spacing increases, the undulation frequency must decrease to maintain both maximal speed and efficiency. Surprisingly, the opposite of this trend is observed in the biological experiments.

3.4. Regime IV: Small ($S \sim 1$) and Fast ($I \gg 1$)

We are not aware of any digging organisms in regime IV, which is surprising because biology generally does an exceptional job exploring and inhabiting all possible corners of phase space. To determine whether this regime is physiologically feasible, we consider the following order-of-magnitude estimate. In this regime, one obtains $L \sim d$ and $\dot{\gamma}L/\sqrt{P/\rho} > 10^{-3}$. The density of a sand grain is typically on the order of 2,500 kg/m³, and the typical stress generated by muscle (which sets a scale for pressure) is approximately 100 kPa. If we now consider grain sizes on the order of 1 mm, an organism would need to shear the surrounding grains at a rate greater than 20 Hz in order to access regime IV. As a baseline for comparison, *C. elegans* oscillates at approximately

1 Hz, and swimming microorganisms may attain frequencies of 20–50 Hz. From this perspective, it appears that the lower bound of the dense flow region may be at the edge of what is physiologically attainable.

4. OUTLOOK

There have been at least two exciting recent theoretical developments and a number of experimental advances that could potentially transform the landscape of digging research. In the first, on the experimental front, we note that the decreasing cost of X-ray detectors and automated tracking software should allow researchers to expand their exploration of the behaviors of organisms in the laboratory and even in the field.

On the theoretical side, there have been several recent efforts by multiple research groups to use the tools of geometric mechanics to visualize kinematic landscapes and to quickly and cheaply determine optimal locomotion strategies (Avron & Raz 2008, Hatton et al. 2011, Melli & Rowley 2010). As described in Section 3.2.1, these techniques have already begun to make inroads into the analysis of simple digging systems (Hatton et al. 2013). Results from these early studies are quite promising and lay the groundwork for future exploration.

The second potentially significant theoretical development is the recognition and implementation of a new constitutive model for granular systems. The cases described above have relied heavily on modified RFTs rather than models derived from the local rheology theory introduced in Section 1.2. This route has not been widely pursued because local rheology models—which perform admirably for fast, dense, uniform flows—encounter problems in nonuniform situations. However, recent developments have led to the derivation of a nonlocal rheology model in which flow at a point is affected by both the local stress and the flow in neighboring material (Henann & Kamrin 2013). The physical notion behind these nonlocal approaches is that mesoscopic regions of material may undergo local elastic deformation, followed by plastic yielding and relaxation to a new local equilibrium position. The interactions between these regions are coupled and yield events at one location may induce elastic modifications in nearby regions. Initial tests of the predictive capability of this nonlocal model are extremely promising: With a single experimentally measured parameter, the model quantitatively predicts hundreds of experimental flows in different geometries, including all the salient features of split-bottom flow, a geometry that has resisted modeling efforts for nearly a decade.

DISCLOSURE STATEMENT

The authors are not aware of any biases that might be perceived as affecting the objectivity of this review.

ACKNOWLEDGMENTS

A.E.H. acknowledges support from the Army Research Office (ARO) under grant W911NF-11-C-0201 and the Defense Advanced Research Projects Agency (DARPA) under grant W31P40-13-1-0013. D.I.G. acknowledges support from the Burroughs Wellcome Fund Career Award at the Scientific Interface, NSF Physics of Living Systems grants PHY-0749991 and PHY-1150760, the Army Research Laboratory (ARL) Micro Autonomous Systems and Technology (MAST) Collaborative Technology Alliance (CTA) under cooperative agreement W911NF-08-2-0004 and the Army Research Office under grant W911NF-11-1-0514. Both authors would like to thank their many students and collaborators for their contributions, including Robin Deits, Yang

Ding, Daniel Dorsch, Nick Gravish, Sunny Jung, Chen Li, Ryan Maladen, Sarah Sharpe, Paul Umbanhowar, and Amos Winter.

LITERATURE CITED

- Attum O, Eason P, Cobbs G. 2007. Morphology, niche segregation, and escape tactics in a sand dune lizard community. *J. Arid Environ.* 68:564–73
- Avron JE, Kenneth O, Oaknin DH. 2005. Pushmepullyou: an efficient micro-swimmer. *New J. Phys.* 7:234
- Avron JE, Raz O. 2008. A geometric theory of swimming: Purcell's swimmer and its symmetrized cousin. *New J. Phys.* 10:063016
- Bagnold RA. 1954. Experiments on a gravity-free dispersion of large solid spheres in a Newtonian fluid under shear. *Proc. R. Soc. Lond. A* 225:49–63
- Batchelor GK, Green JT. 1972. The hydrodynamic interaction of two small freely-moving spheres in a linear flow field. *J. Fluid Mech.* 56:375–400
- Becker LE, Koehler SA, Stone HA. 2003. On self-propulsion of micro-machines at low Reynolds number: Purcell's three-link swimmer. *J. Fluid Mech.* 490:15–35
- Bloch AM. 2003. *Nonholonomic Mechanics and Control*. New York: Springer
- Ding Y, Gravish N, Goldman DI. 2011. Drag induced lift in granular media. *Phys. Rev. Lett.* 106:028001
- Ding Y, Sharpe SS, Masse A, Goldman DI. 2012. Mechanics of undulatory swimming in a frictional fluid. *PLoS Comput. Biol.* 8:e1002810
- Dorgan KM, Arwade SR, Jumars PA. 2007. Burrowing in marine muds by crack propagation: kinematics and forces. *J. Exp. Biol.* 210:4198–212
- Dorgan KM, Jumars PA, Johnson B, Boudreau BP, Landis E. 2005. Burrowing mechanics: burrow extension by crack propagation. *Nature* 433:475
- Eilers H. 1941. Die viscosität von emulsionen hochviskoser stoffe als funktion der konzentration. *Kolloid Z.* 97:313–21
- Einstein A. 1906. Eine neue bestimmung der moleküldimensionen. *Ann. Phys.* 19:289–306
- Ferrini F, Ercolani D, de Cindio B, Nicodemo L, Nicolais L, Ranaudo S. 1979. Shear viscosity of settling suspensions. *Rheol. Acta* 18:289–96
- Forterre Y, Pouliquen O. 2009. Granular flows. *Sémin. Poincaré* 13:69–100
- Fraenkel GV. 1927. Die grabbewegung der soleniden. *Z. Vgl. Physiol.* 6:167–220
- Frankel NA, Acrivos A. 1967. On the viscosity of a concentrated suspension of solid spheres. *Chem. Eng. Sci.* 22:847–53
- Gidmark NJ, Strother JA, Horton JM, Summers AP, Brainerd EL. 2011. Locomotory transition from water to sand and its effects on undulatory kinematics in sand lances (Ammodontidae). *J. Exp. Biol.* 214:657–64
- Goldman D, Komsuoglu H, Koditschek D. 2009. March of the sandbots: a new generation of legged robots will navigate the world's trickiest terrain. *IEEE Spectrum* 46(4):30–35
- Gravish N, Garcia M, Mazouchova N, Levy L, Umbanhowar PB, et al. 2012. Effects of worker size on the dynamics of fire ant tunnel construction. *J. R. Soc. Interface* 9:3312–22
- Gray J, Hancock GJ. 1955. The propulsion of sea-urchin spermatozoa. *J. Exp. Biol.* 32:802–14
- Hatton RL, Burton LJ, Hosoi A, Choset H. 2011. Geometric maneuverability with applications to low Reynolds number swimming. *Proc. 2011 IEEE/RSJ Int. Conf. Intell. Robots Syst. (IROS)*, pp. 3893–98. New York: IEEE
- Hatton RL, Choset H. 2011. Geometric motion planning: the local connection, Stokes' theorem, and the importance of coordinate choice. *Int. J. Robot. Res.* 30:988–1014
- Hatton RL, Ding Y, Choset H, Goldman DI. 2013. Geometric visualization of self-propulsion in a complex medium. *Phys. Rev. Lett.* 110:078101
- Henann DL, Kamrin K. 2013. A predictive, size-dependent continuum model for dense granular flows. *Proc. Natl. Acad. Sci. USA* 110:6730–35
- Holland AF, Dean JM. 1977. The biology of the stout razor clam *Tagelus plebeius*: I. Animal-sediment relationships, feeding mechanism, and community biology. *Chesapeake Sci.* 18:58–66

- Jayne BC, Daggy MW. 2000. The effects of temperature on the burial performance and axial motor pattern of the sand-swimming of the Mojave fringe-toed lizard *Uma scoparia*. *J. Exp. Biol.* 203:1241–52
- Jung S. 2010. *Caenorhabditis elegans* swimming in a saturated particulate system. *Phys. Fluids* 22:031903
- Jung S, Mareck K, Fauci L, Shelley MJ. 2007. Rotational dynamics of a superhelix towed in a Stokes fluid. *Phys. Fluids* 19:103105
- Jung S, Winter AG, Hosoi A. 2011. Dynamics of digging in wet soil. *Int. J. Non-Linear Mech.* 46:602–6
- Krieger IM, Dougherty TJ. 1959. A mechanism for non-Newtonian flow in suspensions of rigid spheres. *Trans. Soc. Rheol.* 3:137–52
- Kudrolli A. 2008. Granular matter: sticky sand. *Nat. Mater.* 7:174–75
- Kuo AD. 2007. Choosing your steps carefully. *IEEE Robot. Automat. Mag.* 14(2):18–29
- Lambe T, Whitman R. 1969. *Soil Mechanics*. New York: Wiley
- Landau LD, Lifshitz E. 1984. *Theory of Elasticity*. Oxford, UK: Butterworth-Heinemann. 3rd ed.
- Lauga E. 2007. Floppy swimming: viscous locomotion of actuated elastica. *Phys. Rev. E* 75:041916
- Lauga E. 2011. Life around the scallop theorem. *Soft Matter* 7:3060–65
- Lauga E, Powers TR. 2009. The hydrodynamics of swimming microorganisms. *Rep. Prog. Phys.* 72:096601
- Li C, Zhang T, Goldman DI. 2013. A terradynamics of legged locomotion on granular media. *Science* 339:1408–12
- Liu B, Powers TR, Breuer KS. 2011. Force-free swimming of a model helical flagellum in viscoelastic fluids. *Proc. Natl. Acad. Sci. USA* 108:19516–20
- Majmudar T, Keaveny EE, Zhang J, Shelley MJ. 2012. Experiments and theory of undulatory locomotion in a simple structured medium. *J. R. Soc. Interface* 9:1809–23
- Maladen RD, Ding Y, Li C, Goldman DI. 2009. Undulatory swimming in sand: subsurface locomotion of the sandfish lizard. *Science* 325:314–18
- Maladen RD, Ding Y, Umbanhowar PB, Goldman DI. 2011a. Undulatory swimming in sand: experimental and simulation studies of a robotic sandfish. *Int. J. Robot. Res.* 30:793–805
- Maladen RD, Ding Y, Umbanhowar PB, Kamor A, Goldman DI. 2011b. Mechanical models of sandfish locomotion reveal principles of high performance subsurface sand-swimming. *J. R. Soc. Interface* 8:1332–45
- Maron SH, Pierce PE. 1956. Application of Ree-Eyring generalized flow theory to suspensions of spherical particles. *J. Colloid Sci.* 11:80–95
- Melli J, Rowley CW. 2010. Models and control of fish-like locomotion. *Exp. Mech.* 50:1355–60
- Metcalfe E. 2007. *The Wit and Wisdom of Denis Healey*. Milton Keynes, UK: AuthorHouse
- Mosauer W. 1932. Adaptive convergence in the sand reptiles of the Sahara and of California: a study in structure and behavior. *Copeia* 1932:72–78
- Norris KS, Kavanau JL. 1966. The burrowing of the western shovel-nosed snake, *Chionactis occipitalis* Hallowell, and the undersand environment. *Copeia* 1966:650–64
- Ostrowski J, Burdick J. 1998. The geometric mechanics of undulatory robotic locomotion. *Int. J. Robot. Res.* 17:683–701
- Park S, Hwang H, Martinez F, Austin RH, Ryu WS. 2008. Enhanced *Caenorhabditis elegans* locomotion in a structured microfluidic environment. *PLoS ONE* 3:e2550
- Poschel T. 2005. *Computational Granular Dynamics: Models and Algorithms*. Berlin: Springer-Verlag
- Purcell EM. 1977. Life at low Reynolds number. *Am. J. Phys.* 45:3–11
- Qian B, Powers TR, Breuer KS. 2008. Shape transition and propulsive force of an elastic rod rotating in a viscous fluid. *Phys. Rev. Lett.* 100:078101
- Raz O, Avron JE. 2008. A comment on optimal stroke patterns for Purcell’s three-link swimmer. *Phys. Rev. Lett.* 100:029801
- Rodenborn B, Chen CH, Swinney HL, Liu B, Zhang H. 2013. Propulsion of microorganisms by a helical flagellum. *Proc. Natl. Acad. Sci. USA* 110:E338–47
- Shapere A, Wilczek F. 1987. Self-propulsion at low Reynolds number. *Phys. Rev. Lett.* 58:2051–54
- Sharpe SS, Ding Y, Goldman DI. 2012. Environmental interaction influences muscle activation strategy during sand-swimming in the sandfish lizard *Scincus scincus*. *J. Exp. Biol.* 216:260–74
- Sharpe SS, Koehler SA, Kuckuk R, Serrano M, Vela P, Goldman DI. 2014a. Locomotor advantages of being a slender and slick sand swimmer. *J. Exp. Biol.* Manuscript in review

- Sharpe SS, Kuckuk R, Goldman DI. 2014b. Locomotion of the ocellated skink in wet granular media. *J. R. Soc. Interface*. Manuscript in preparation
- Tam D, Hosoi AE. 2007. Optimal stroke patterns for Purcell's three-link swimmer. *Phys. Rev. Lett.* 98:068105
- Taylor GI. 1951. Analysis of the swimming of microscopic organisms. *Proc. R. Soc. A* 209:447–61
- Terzaghi K, Peck R, Mesri G. 1996. *Soil Mechanics in Engineering Practice*. New York: Wiley. 3rd ed.
- Trueman ER. 1967. The dynamics of burrowing in *Ensis* (bivalvia). *Proc. R. Soc. Lond. B* 166:459–76
- Trueman ER. 1975. *The Locomotion of Soft-Bodied Animals*. Amsterdam: Elsevier
- Wiegardt K. 1975. Experiments in granular flow. *Annu. Rev. Fluid Mech.* 7:89–114
- Wiggins CH, Goldstein RE. 1998. Flexive and propulsive dynamics of elastica at low Reynolds number. *Phys. Rev. Lett.* 80:3879–82
- Winter AG, Deits RLH, Dorsch DS, Slocum AH, Hosoi AE. 2014. Razor clam to RoboClam: burrowing drag reduction mechanisms and their robotic adaptation. *Bioinspir. Biomim.* 9:036009
- Winter AG, Deits RLH, Hosoi AE. 2012. Localized fluidization burrowing mechanics of *Ensis directus*. *J. Exp. Biol.* 215:2072–80
- Yang J, Wolgemuth CW, Huber G. 2009. Kinematics of the swimming of *Spiroplasma*. *Phys. Rev. Lett.* 102:218102
- Yu TS, Lauga E, Hosoi AE. 2006. Experimental investigations of elastic tail propulsion at low Reynolds number. *Phys. Fluids* 18:091701



Contents

Fluid Mechanics in Sommerfeld's School <i>Michael Eckert</i>	1
Discrete Element Method Simulations for Complex Granular Flows <i>Yu Guo and Jennifer Sinclair Curtis</i>	21
Modeling the Rheology of Polymer Melts and Solutions <i>R.G. Larson and Priyanka S. Desai</i>	47
Liquid Transfer in Printing Processes: Liquid Bridges with Moving Contact Lines <i>Satish Kumar</i>	67
Dissipation in Turbulent Flows <i>J. Christos Vassilicos</i>	95
Floating Versus Sinking <i>Dominic Vella</i>	115
Langrangian Coherent Structures <i>George Haller</i>	137
Flows Driven by Libration, Precession, and Tides <i>Michael Le Bars, David Cébron, and Patrice Le Gal</i>	163
Fountains in Industry and Nature <i>G.R. Hunt and H.C. Burridge</i>	195
Acoustic Remote Sensing <i>David R. Dowling and Karim G. Sabra</i>	221
Coalescence of Drops <i>H. Pirouz Kavehpour</i>	245
Pilot-Wave Hydrodynamics <i>John W.M. Bush</i>	269
Ignition, Liftoff, and Extinction of Gaseous Diffusion Flames <i>Amable Liñán, Marcos Vera, and Antonio L. Sánchez</i>	293
The Clinical Assessment of Intraventricular Flows <i>Javier Bermejo, Pablo Martínez-Legazpi, and Juan C. del Álamo</i>	315

Green Algae as Model Organisms for Biological Fluid Dynamics <i>Raymond E. Goldstein</i>	343
Fluid Mechanics of Blood Clot Formation <i>Aaron L. Fogelson and Keith B. Neeves</i>	377
Generation of Microbubbles with Applications to Industry and Medicine <i>Javier Rodríguez-Rodríguez, Alejandro Sevilla, Carlos Martínez-Bazán, and José Manuel Gordillo</i>	405
Beneath Our Feet: Strategies for Locomotion in Granular Media <i>A.E. Hosoi and Daniel I. Goldman</i>	431
Sports Ballistics <i>Christophe Clanet</i>	455
Dynamic Stall in Pitching Airfoils: Aerodynamic Damping and Compressibility Effects <i>Thomas C. Corke and Flint O. Thomas</i>	479
Ocean Spray <i>Fabrice Veron</i>	507
Stability of Constrained Capillary Surfaces <i>J.B. Bostwick and P.H. Steen</i>	539
Mixing and Transport in Coastal River Plumes <i>Alexander R. Horner-Devine, Robert D. Hetland, and Daniel G. MacDonald</i>	569

Indexes

Cumulative Index of Contributing Authors, Volumes 1–47	595
Cumulative Index of Article Titles, Volumes 1–47	605

Errata

An online log of corrections to *Annual Review of Fluid Mechanics* articles may be found at <http://www.annualreviews.org/errata/fluid>